PHYSICAL REVIEW B **100**, 134438 (2019)

Magnetic anisotropy of the two-dimensional ferromagnetic insulator $MnBi_2Te_4$

Yang Li,[1,2] Zeyu Jiang,[1,2] Jiaheng Li,[1,2] Shengnan Xu,[1,2] and Wenhui Duan[1,2,3,*]
[1]*State Key Laboratory of Low Dimensional Quantum Physics, Department of Physics, Tsinghua University, Beijing 100084, People's Republic of China*
[2]*Collaborative Innovation Center of Quantum Matter, Beijing 100084, People's Republic of China*
[3]*Institute for Advanced Study, Tsinghua University, Beijing 100084, People's Republic of China*

(Received 16 July 2019; published 31 October 2019)

Magnetic anisotropy is vital for establishing the long-range magnetic order in two-dimensional systems. Here, based on the density functional theory calculation, we systematically study the magnetic anisotropy of monolayer $MnBi_2Te_4$, a ferromagnetic insulator. We find that the exchange interaction in monolayer $MnBi_2Te_4$ is nearly isotropic and almost has no contribution to the magnetic anisotropy, as a result of the weak *p-d* hybridization between Mn and Te atoms. We further reveal that magnetic anisotropy originates from single-ion anisotropy, leading to a ferromagnetic Curie temperature of about 20 K. Interestingly, the emergence of single-ion anisotropy cannot be induced solely by the spin-orbit coupling of Mn atoms, but also involves the spin-orbit coupling of ligand Te, as the spin-orbit coupling of Te atoms can induce changes in the local Mn-*d* states. This behavior is very different from that in monolayer CrI_3 and $CrGeTe_3$, where the anisotropy of the exchange interaction is critical for long-range magnetic order. Our findings may provide a comprehensive understanding of the magnetic behavior in monolayer $MnBi_2Te_4$ and motivate further research on its potential applications.

DOI: 10.1103/PhysRevB.100.134438

I. INTRODUCTION

Two-dimensional (2D) materials provide an ideal platform to explore interesting physical phenomena as well as plenty of candidates to design next generation functional devices [1–4]. Among numerous 2D materials, no intrinsic magnet had been found until the long-range magnetic order was experimentally observed recently in some atomically thin materials, such as the insulating ferromagnets CrI_3 [5] and $CrGeTe_3$ [6], the itinerant ferromagnet Fe_3GeTe_2 [7], the antiferromagnet $FePS_3$ [8,9], and the room-temperature ferromagnets VSe_2 [10] and $MnSe_x$ [11]. On one hand, the magnetic phases and anisotropy of these 2D materials can be manipulated via an external electric field [12–15], creating other opportunities for the applications of spintronics and nanoelectronics. On the other hand, long-range magnetic order breaks the time-reversal symmetry of these materials, leading to the emergence of some unique quantum states, such as the intrinsic quantum anomalous Hall state [16,17], giant valley splitting [18], and the half-excitonic insulator [19] predicted in 2D ferromagnetic (FM) transition metal halides. Undoubtedly, the discovery of intrinsic 2D magnetic materials has brought vitality to the research of 2D materials [20].

$MnBi_2Te_4$, experimentally synthesized in 2013 [21], is a typical van der Waals layered magnetic material. The tetradymite-type $MnBi_2Te_4$ is composed of FM septuple-layer blocks stacked in the antiferromagnetic (AFM) coupling, and was reported to be the first AFM topological insulator not long ago [22–25]. Moreover, other topological phases can also exist in this material, including the type-II Weyl semimetal state in FM $MnBi_2Te_4$ [25] and the quantum anomalous Hall effect in $MnBi_2Te_4$ thin films [25–28]. Interestingly, FM order was predicated to persist in one septuple-layer block exfoliated from the bulk $MnBi_2Te_4$ [25,26], implying monolayer $MnBi_2Te_4$ is a promising 2D magnetic material. Because the rich topological states in $MnBi_2Te_4$ are closely related to the magnetic properties of each layer, it is important to clarify the magnetic mechanism of monolayer $MnBi_2Te_4$, which is also a key question from the viewpoint of 2D magnetism. However, the magnetic anisotropy of monolayer $MnBi_2Te_4$, which is essential for establishing long-range magnetic order in 2D systems, has not yet been comprehensively studied.

The main purpose of this paper is to systematically understand the magnetic anisotropy of monolayer $MnBi_2Te_4$. In general, several factors with complex synergy or competition can contribute to magnetic anisotropy, leading to various magnetic behaviors in different materials [29–31]. In order to identify the key factor that causes the magnetic anisotropy in monolayer $MnBi_2Te_4$, we calculated all elements of the coupling matrices in the general spin lattice Hamiltonian, using the density functional theory (DFT) calculation. We find the exchange interaction in monolayer $MnBi_2Te_4$ can be described by an isotropic Heisenberg Hamiltonian, and the superexchange interaction is dominant for this isotropic exchange interaction while the direct exchange interaction is negligible in monolayer $MnBi_2Te_4$. Then we study in detail the single-ion anisotropy which is caused by the spin-orbit coupling (SOC) effect and induces magnetic anisotropy. Based on the spin lattice Hamiltonian we obtained, the Curie temperature (T_c) of monolayer $MnBi_2Te_4$ is also estimated using the self-consistent spin-wave theory [32]. At the end of this paper, we extend our investigation to other isostructural systems such as $MnSb_2Te_4$ and $MnBi_2Se_4$, discussing the

---

[*] dwh@phys.tsinghua.edu.cn

differences and similarities of the magnetic anisotropy in these monolayer $MnBi_2Te_4$-like systems.

II. METHODS

Our DFT calculations were performed using the Vienna *ab initio* simulation package (VASP) [33] with the Perdew-Burke-Ernzerhof functional [34] used to approximate the exchange-correlation functional. The projector augmented-wave method [35] was employed to treat the core electrons, while Bi 6s and 6p states, Mn 3p, 4s, and 3d states, and Te 5s and 5p states were considered to be the valence electrons. A 350-eV energy cutoff for the plane-wave basis was employed, and a 15-Å vacuum layer was used to avoid the interactions from the periodic images. An $18 \times 18 \times 1$ Γ centered k-point mesh over the first Brillouin zone was employed. Here, the partly occupied 3d orbitals of Mn atoms were treated using the generalized gradient approximation (GGA)+U approach introduced by Dudarev *et al.* [36] with the effective Hubbard U_{eff} chosen to be 3.0, 4.0, and 5.0 eV, all of which led to the same results, qualitatively. Therefore, the results corresponding to $U_{\mathrm{eff}} = 3.0$ eV are presented in the main text and the results of other choices are summarized in the Supplemental Material [37]. The magnetic exchange coupling parameters and single-ion anisotropy parameters were obtained using the four-state energy-mapping analysis [38,39], where a $3 \times 3 \times 1$ supercell combined with the $4 \times 4 \times 1$ k-point mesh were used to perform calculations. We also performed test calculations employing the denser $6 \times 6 \times 1$ k-point mesh and a larger $4 \times 4 \times 1$ supercell, which yielded the same results as shown in Table S1 [37].

III. RESULTS AND DISCUSSION

Monolayer $MnBi_2Te_4$, i.e., one septuple-layer block, is crystallized in the $P\bar{3}m1$ space group. As shown in Fig. 1(a), monolayer $MnBi_2Te_4$ consists of seven atomic layers with the sequence of Te-Bi-Te-Mn-Te-Bi-Te. Figures 1(b) and 1(c) show the structure of the Te-Mn-Te layer in the middle of the septuple-layer block. The Te atoms form edge-sharing octahedral cages and the centered Mn atoms form a triangular lattice. The optimized in-plane lattice constant is 4.36 Å, slightly larger than that of its bulk phase [21]. Five unpaired Mn-3d electrons with a total spin $S = 5/2$ provide the magnetism of monolayer $MnBi_2Te_4$, and the band structure of the FM ground state with the SOC effect is shown in Fig. 1(d). Due to the threefold rotational symmetry, the d states of Mn atoms split into three groups according to the absolute value of the magnetic quantum number m_z [40], and all of them are localized far away from the Fermi level. Therefore, it is reasonable to expect that the magnetism of monolayer $MnBi_2Te_4$ is relatively robust and hard to manipulate using the conventional experimental approaches such as applying strain and charge doping [41], which mainly influence the properties of the electrons near the Fermi level. This feature is in sharp contrast to monolayer CrI_3 [42,43] and $CrGeTe_3$ [44,45], where the d states of transition metal atoms also have a large weight around the Fermi level. The magnetic anisotropy energy (MAE) calculation shows that the z direction is the preferred spin orientation in monolayer $MnBi_2Te_4$ [25,26]. In the following, we will discuss which effect contributes to this easy-axis magnetic anisotropy and leads to the long-range FM order in monolayer $MnBi_2Te_4$.

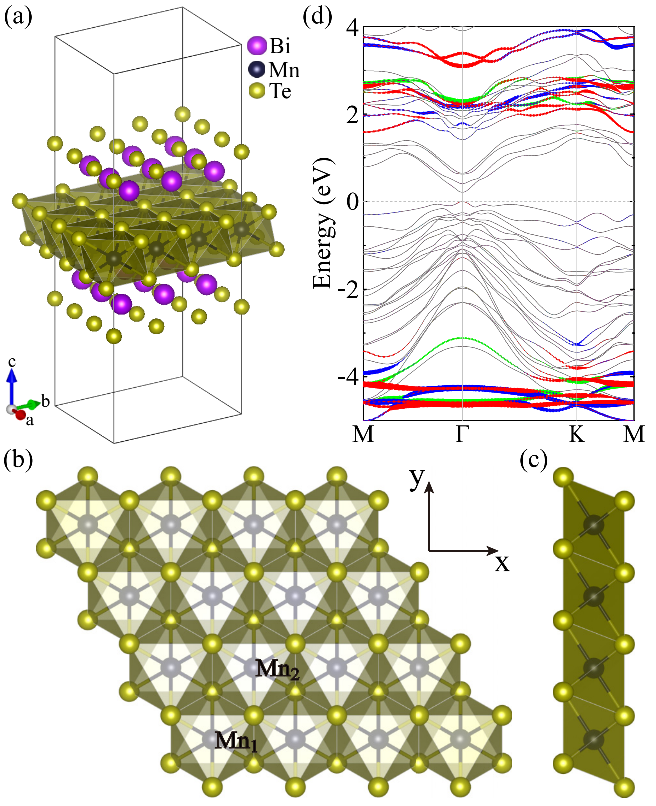

FIG. 1. (a) The crystal structure of monolayer $MnBi_2Te_4$. The light blue, deep blue, and green balls represent Bi, Mn, and Te atoms, respectively. (b), (c) The top and side views of the Te-Mn-Te layer located in the middle of the septuple-layer block. (d) The SOC band structure of the FM monolayer $MnBi_2Te_4$. The red, blue, and green dots represent the projections onto the d_{xy,x^2-y^2}, $d_{yz,xz}$, and d_{z^2} states of the Mn atom, respectively.

Because the d atomic states of Mn atoms are extremely localized [as shown in Fig. 1(d)], the general form of the spin Hamiltonian of monolayer $MnBi_2Te_4$ can be written as

$$H = \frac{1}{2}\sum_{i,j} \mathbf{S}_i \mathcal{J}_{ij} \mathbf{S}_j + \sum_{i} \mathbf{S}_i \mathcal{A}_i \mathbf{S}_i, \qquad (1)$$

where $\mathbf{S}_i$ represents the spin operator in site i. The first term describes the exchange interaction, including the symmetric exchange interaction and the Dzyaloshinskii-Moriya (DM) interaction [46,47]. The second term is the single-ion anisotropy (SIA) term. Here, $\mathcal{J}_{ij}$ and $\mathcal{A}_i$ are the 3×3 matrices whose elements can be determined by the DFT calculation.

Let us first look at the exchange interaction term whose coupling matrix $\mathcal{J}_{ij}$ is expressed in Cartesian coordinates. Among the six nearest neighbors of the Mn_1 atom, we calculated the nearest-neighbor exchange coupling matrix $\mathcal{J}_{12}$ of the Mn_1-Mn_2 pair shown in Fig. 1(b), and list the corresponding matrix elements in Table I. The other five nearest-neighbor exchange coupling matrices can be obtained through the threefold rotational operation with respect to the z direction and the translational operation along the lattice vectors. As

TABLE I. The exchange coupling matrix $\mathcal{J}_{12}$ of the Mn_1-Mn_2 pair in units of meV. All matrix elements shown here are calculated using the DFT+U+SOC method with $U_{\mathrm{eff}} = 3.0$ eV.

$\mathcal{J}_{12}^{xx}$	$\mathcal{J}_{12}^{yy}$	$\mathcal{J}_{12}^{zz}$	$\mathcal{J}_{12}^{xy}$, $\mathcal{J}_{12}^{yx}$	$\mathcal{J}_{12}^{xz}$, $\mathcal{J}_{12}^{zx}$	$\mathcal{J}_{12}^{yz}$, $\mathcal{J}_{12}^{zy}$
−1.37	−1.39	−1.38	−0.02	0.00	0.00

one can see, the exchange coupling matrix $\mathcal{J}_{12}$ approximates to a diagonal matrix with three identical diagonal elements when we neglect the tiny numerical differences whose contribution to the magnetic anisotropy is trifling, resulting in $\mathcal{J}_{ij} = \mathcal{J}_{12}$ for any nearest-neighbor Mn pairs i, j. As a result, the symmetric part of the nearest-neighbor exchange coupling matrix expressed as

$$H_{\mathrm{EX}}^{S} = \frac{1}{2}\sum_{\langle i,j\rangle}\sum_{\alpha,\beta}\frac{1}{2}\left(\mathcal{J}_{ij}^{\alpha\beta} + \mathcal{J}_{ij}^{\beta\alpha}\right)S_i^{\alpha}S_j^{\beta}, \tag{2}$$

with $\alpha, \beta = x, y, z$ referring to the component indices in Cartesian coordinates, can be further reduced into a much simpler form,

$$H_{\mathrm{EX}}^{S} = \frac{1}{2}\sum_{\langle i,j\rangle} J\mathbf{S}_i \cdot \mathbf{S}_j, \tag{3}$$

where $\langle\,\rangle$ denotes the summation is over all nearest-neighbor sites i, j, and parameter J is the average of $\mathcal{J}_{12}^{xx}$, $\mathcal{J}_{12}^{yy}$, and $\mathcal{J}_{12}^{zz}$. Equation (3) is the well-known isotropic Heisenberg Hamiltonian with the FM coupling parameter ($J < 0$). The antisymmetric part, which is written as

$$H_{\mathrm{EX}}^{A} = \frac{1}{2}\sum_{\langle i,j\rangle}\sum_{\alpha,\beta}\frac{1}{2}\left(\mathcal{J}_{ij}^{\alpha\beta} - \mathcal{J}_{ij}^{\beta\alpha}\right)S_i^{\alpha}S_j^{\beta}, \tag{4}$$

represents the DM interaction. The zero off-diagonal elements cause the DM interaction to be zero for monolayer $MnBi_2Te_4$, which is consistent with the restriction of the inversion symmetry [47]. Therefore, the nearest-neighbor exchange interaction can be described using the spin Hamiltonian in Eq. (3). This is different from the cases of monolayer CrI_3 and $CrGeTe_3$ where the anisotropy of the exchange interaction plays an important role for the long-range FM order [29,30].

The second-nearest-neighbor exchange coupling matrices were also calculated and found to be two orders smaller than the nearest-neighbor exchange interaction. Therefore, we neglect the exchange interactions of the second-nearest-neighbor Mn atomic pairs and more distant Mn atomic pairs in this work.

It is unexpected that the exchange interaction is nearly isotropic in a 2D system where the in-plane and out-of-plane directions are clearly inequivalent. In order to understand this feature, we first analyze the mechanism of the exchange interaction in monolayer $MnBi_2Te_4$. Figure 2(a) presents the energy difference of monolayer $MnBi_2Te_4$ between the stripy-type AFM/zigzag-type AFM and FM configurations as well as the corresponding Mn-Te-Mn bond angle at different biaxial strains. Herein, the three different magnetic configurations are shown in Fig. 2(b). It can be seen that the bond angle gradually approaches 90° from the tensile strain to compressive strain, and the ferromagnetism is enhanced at the same time. This behavior originates from the superexchange interaction according to the Goodenough-Kanamori rule [48–50]. On the other hand, the energy difference decreases when the applied compressive strain exceeds 3.5%, as shown in Fig. 2(a). This probably originates from the enhancement of the AFM direct exchange interaction, corresponding to a weakening of the ferromagnetic coupling of monolayer $MnBi_2Te_4$. This behavior remains unchanged when the SOC is taken into account [37]. Therefore, the exchange interaction is mainly contributed by the near 90° superexchange interaction, and the effect of the direct exchange interaction is negligible for the freestanding monolayer $MnBi_2Te_4$.

As the superexchange interaction is dominant for the exchange interaction, the p-d hybridization between Mn and the Te atoms near the Mn atomic layer (i.e., inner Te) is crucial to

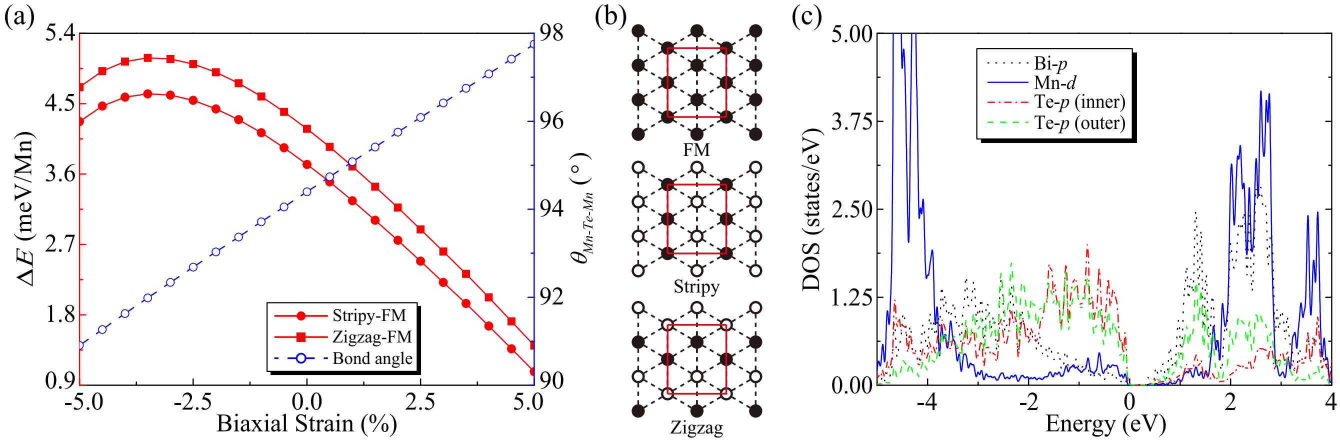

FIG. 2. (a) The energy difference between the stripy-type AFM (red solid circles)/zigzag-type AFM (red solid squares) and FM configurations as a function of biaxial strain. The blue open circles represent the evolution of the Mn-Te-Mn bond angle at different biaxial strains. (b) The schematic top views of the FM, stripy, and zigzag magnetic configurations. The solid and open circles represent the spin-up and spin-down states, respectively. The red rectangle indicates the unit cell used to perform calculations. (c) The PDOS of monolayer $MnBi_2Te_4$ with the SOC effect. The black dotted line, blue solid line, red dashed-dotted line, and green dashed line, respectively, represent the p states of Bi, d states of Mn, p states of the inner Te, and p states of the outer Te.

understand the feature of the isotropic exchange interaction in monolayer $MnBi_2Te_4$. Figure 2(c) shows the partial density of states (PDOS) including the SOC effect. Unexpectedly, there is only weak hybridization between the d states of Mn and p states of inner Te. Although changing the spin orientation will affect the local charge distribution around the Mn atoms through the SOC effect, its influence on the exchange coupling can be extremely weak owing to the small orbital overlap resulting from the lack of efficient p-d hybridization. Meanwhile, the spherical characteristic of the closed Mn-$3d^5$ shell may further suppress the changes in the hopping strength. As a result, the strength of the exchange interactions with different spin orientation configurations is nearly the same. Besides, the small orbital overlap also causes a relatively weak exchange interaction, which is the one reason for the low critical temperature of monolayer $MnBi_2Te_4$, as discussed later in this paper. In contrast, the p-d hybridization in monolayer CrI_3 and $CrGeTe_3$ is significant [37,42–45], and the considerable mixing between the d orbitals of Cr and p orbitals of ligand (I or Te) causes the strength of the electron hopping to be sensitive to the spin orientation, resulting in a remarkable anisotropy of the exchange interaction.

The 2D isotropic Heisenberg spin Hamiltonian, as proved by Mermin and Wagner [51], cannot establish long-range magnetic order at a finite temperature. Therefore, the presence of the FM order in monolayer $MnBi_2Te_4$ is closely related to the SIA, requiring a separate analysis of the second term (i.e., SIA) in Eq. (1). We calculated the SIA of the Mn atom, and found that the coupling matrix $\mathcal{A}$ is diagonal with $\mathcal{A}^{yy} = \mathcal{A}^{xx}$ and $\mathcal{A}^{zz} - \mathcal{A}^{xx} = -0.18$ meV. As a result, the second term of Eq. (1) can be reduced into

$$H_{\mathrm{SIA}} = \sum_i A S_i^z S_i^z, \tag{5}$$

where $A = \mathcal{A}^{zz} - \mathcal{A}^{xx}$. The negative A indicates the SIA prefers the z direction, which leads to out-of-plane magnetism as confirmed by the MAE calculation.

It was recently suggested that the SIA may be caused by the SOC of the nonmagnetic atoms instead of by the magnetic atoms themselves [29,30]. To understand the origin of the SIA in monolayer $MnBi_2Te_4$, we performed the atom-resolved SIA calculations by changing the SOC strength of the atoms separately. As shown in Fig. 3(a), when we take into account only one kind of the element's SOC, the SIA is much smaller than that in the real situation (denoted by the black line). In other words, the SOC of each element alone cannot cause the SIA. Actually, the SIA mainly originates from the joint SOC effect of Mn and Te atoms, because the calculated SIA approaches the correct value only when the SOC of the Mn and Te atoms is considered simultaneously [see Fig. 3(b)].

As the Mn-d states are very localized and weakly hybridized with other states, the emergence of SIA must involve the SOC of the Mn atoms themselves. However, only extremely weak SIA can be obtained where considering the SOC of Mn atoms alone. To further understand the enhancement of the SIA caused by the SOC of the Te atoms, we chose the five bands with the largest weight of the Mn-d states as shown in Fig. 1(d) and calculated the corresponding partial charge densities in three different situations: neglecting the SOC (n_0), considering the SOC of Mn atoms (n_1), and including the SOC of Mn and Te atoms (n_2). The differential partial charge densities $\Delta n_{\mathrm{Mn}} = n_1 - n_0$ and $\Delta n_{\mathrm{Te}} = n_2 - n_1$ are shown in Figs. 3(c) and 3(d), respectively. Here, the chosen isosurface level of Δn_{Mn} is 20 times smaller than that of the Δn_{Te} in order to show Δn_{Mn} clearly. Due to the relatively strong SOC, the Te atomic states will have significant changes after taking into account its SOC. This will further induce the changes in the d states of the neighboring Mn atoms. The Δn_{Te} shown in Fig. 3(d) shows that an anisotropic change of the Mn-d states appears after considering the SOC of Te atoms. Importantly, compared to the changes in the Mn-d states caused by the SOC of the Mn atoms themselves [i.e., the Δn_{Mn} shown in Fig. 3(c)], the influences from the SOC of Te atoms is much significant. Therefore, under the precondition of considering the SOC of Mn atoms, the changes in the Mn-d orbitals induced by the SOC of the Te atoms can influence the spin orientation directly and sufficiently, which may be the reason for the enhancement of the SIA in monolayer $MnBi_2Te_4$.

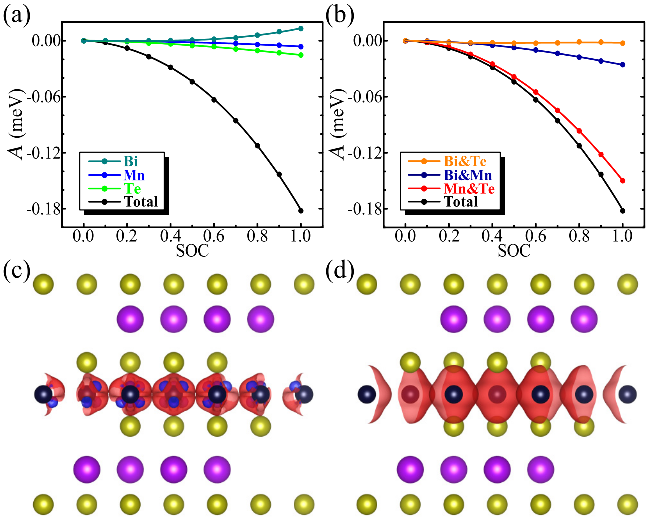

FIG. 3. The atom-resolved SIA parameter A as a function of SOC strength. (a) Only one kind of the element's SOC is considered. (b) Two different kinds of the elements' SOC are included. The black line represents the result taking into account all the elements' SOC. (c) The differential partial charge density Δn_{Mn} of monolayer Bi_2MnTe_4 with and without the SOC of Mn atoms. (d) The differential partial charge density Δn_{Te} of monolayer Bi_2MnTe_4 with the SOC of Mn and Te atoms and with only Mn's SOC. Here, the isosurface level in (c) is 20 times smaller than that in (d).

Now, we get the spin Hamiltonian describing monolayer $MnBi_2Te_4$ as

$$H = \frac{1}{2}\sum_{\langle i,j\rangle} J\mathbf{S}_i \cdot \mathbf{S}_j + \sum_i A S_i^z S_i^z. \tag{6}$$

By performing the Holstein-Primakoff transformation [52] and some straightforward derivations, this spin Hamiltonain can be expanded into a power series in terms of bosonic creation and annihilation operators. The quadratic term of the power series represents the noninteracting magnons with energy dispersion

$$\hbar\omega_k = ZJS(\gamma_k - 1) - 2AS, \tag{7}$$

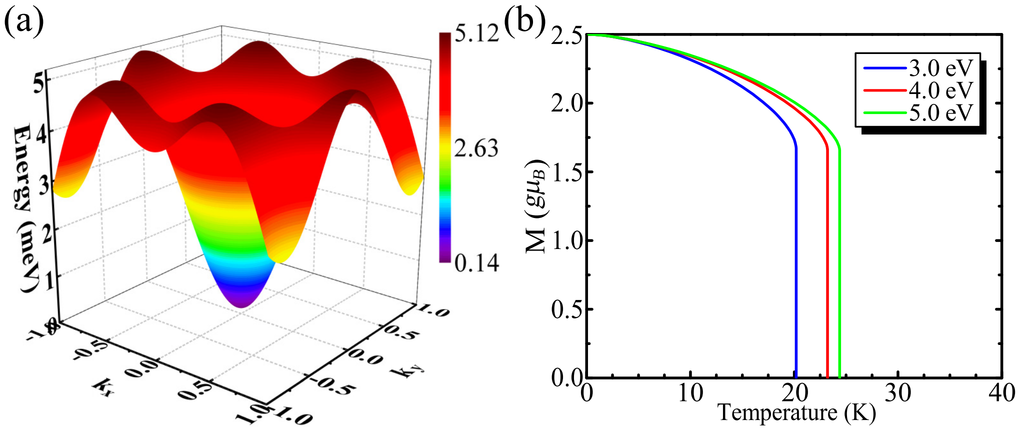

FIG. 4. (a) The magnon dispersion of monolayer $MnBi_2Te_4$ over the first Brillouin zone, where $J = -1.38$ meV and $A = -0.18$ meV. (b) The magnetization curve as a function of temperature. The blue, red, and green lines correspond to the situations with $U_{\rm eff} = 3.0$, 4.0, and 5.0 eV, respectively.

where Z indicates the number of nearest neighbors, S is the total spin quantum number, and $\gamma_k = \sum_\delta e^{i\mathbf{k}\cdot\delta}/Z$ with the summation over all nearest neighbors δ. Figure 4(a) shows the magnon dispersion of monolayer $MnBi_2Te_4$ over the first Brillouin zone. It can be seen that there exists a energy gap $E_g = -2AS = 0.144$ meV at the Γ point. From the spin-wave theory, a gapless magnon dispersion will cause the divergence of the magnetization in one- and two-dimensional systems [20,29,53]. Therefore, a gapped magnon dispersion is required for the appearance of long-range magnetic order. In monolayer $MnBi_2Te_4$, this energy gap is brought by the SIA, clearly. It should be noted that the dispersion gap can originate from different factors such as the anisotropic exchange interaction in monolayer CrI_3 [29]. Although the energy gap causes 2D magnetism, the mechanism behind monolayer $MnBi_2Te_4$ is different from that in other typical 2D magnets.

The quartic term of the power series represents the magnon-magnon interaction which can be diagonalized using the Hartree-Fock approximation [6,53]. After considering the contribution of this higher-order term, the magnon dispersion can be rewritten as

$$\hbar\omega'_k = ZJS(\gamma_k - 1)\zeta - 2AS\xi, \tag{8}$$

where ζ and ξ are the functions of temperature T. Equation (8) illustrates that the magnon-magnon interaction causes the renormalization of the energy dispersion through two temperature relevant factors which are expressed as

$$\begin{aligned}\zeta &= 1 - \frac{1}{SN}\sum_q (1-\gamma_q)\frac{1}{e^{\hbar\omega'_q/k_BT}-1},\\ \xi &= \frac{2S-1}{2S} - \frac{4}{2SN}\sum_q \frac{1}{e^{\hbar\omega'_q/k_BT}-1}.\end{aligned} \tag{9}$$

Because the factors ζ and ξ are dependent on the energy dispersion, Eqs. (8) and (9) can be solved self-consistently with Eq. (7) being used as the initial input energy dispersion. This self-consistent spin-wave approach has been previously used to estimate the T_c of monolayer CrI_3 [29], bilayer $CrGeTe_3$ under external magnetic fields [6], and some model systems [32,53]. Using the coupling parameters extracted by our DFT calculations, we calculated the magnetization curve $M(T)$ of monolayer $MnBi_2Te_4$ as plotted in Fig. 4(b). The T_c's of monolayer $MnBi_2Te_4$ corresponding to $U_{\rm eff} = 3.0, 4.0$, and 5.0 eV are equal to 20, 23, and 24 K, respectively. The relatively low T_c is caused by the weak exchange interaction and small MAE in monolayer $MnBi_2Te_4$ (as a contrast, the exchange coupling parameter and MAE of monolayer CrI_3 are about −2.5 and −0.65 meV, respectively [29,42], and the corresponding T_c is 45 K [5]). Experimentally, the T_c of the seven septuple-layer $MnBi_2Te_4$ thin film was determined to be 20 K through measuring the remnant magnetization [23], which is similar to our estimated T_c of monolayer $MnBi_2Te_4$. Due to the interlayer AFM coupling in $MnBi_2Te_4$, the seven layer $MnBi_2Te_4$ macroscopically carries only one-layer effective remnant magnetization. This is perhaps the reason for the similarity of the T_c in monolayer $MnBi_2Te_4$ and the seven layer $MnBi_2Te_4$ film.

In the end, we extend our discussions to other isostructural systems. $MnSb_2Te_4$ was found to be a topologically trivial magnetic insulator with the same magnetic structure as $MnBi_2Te_4$ in recent works [54,55]. Similar to monolayer $MnBi_2Te_4$, we find that the exchange interaction of monolayer $MnSb_2Te_4$ is also nearly isotropic, and the SIA is the origin of its magnetic anisotropy. The calculated SIA of monolayer $MnSb_2Te_4$ is $A = -0.16$ meV, which is very close to the value of monolayer $MnBi_2Te_4$. As mentioned above, the SIA originates from the SOC of Mn and Te atoms and is almost unrelated to that of Bi atoms. Therefore, it is reasonable that the SIA will not change as the pnictogen changing from Bi to Sb. $MnBi_2Se_4$ is another isostructural material which was predicted to have several topological phases in different magnetic phases [56]. Its magnetic ground state is also an A-type AFM insulator. Different from the monolayer $MnBi_2Te_4$ and $MnSb_2Te_4$, the magnetic anisotropy of monolayer $MnBi_2Se_4$ may be more complicated. As the SOC of Se atoms is weaker than that of the Te atoms, the SIA of monolayer $MnBi_2Se_4$ reduces to −0.07 meV, less than half of that in monolayer $MnBi_2Te_4$ and $MnSb_2Te_4$. This weak SIA is of the same magnitude as the exchange anisotropy, and thus the magnetic anisotropy of monolayer $\mathrm{MnBi_2Se_4}$ should be determined jointly by the exchange anisotropy and SIA in monolayer $\mathrm{MnBi_2Se_4}$.

IV. CONCLUSION

In summary, we systematically investigate the magnetic anisotropy of monolayer $\mathrm{MnBi_2Te_4}$. Different from typical two-dimensional ferromagnetic insulators such as $\mathrm{CrI_3}$ and $\mathrm{CrGeTe_3}$, the exchange interaction in monolayer $\mathrm{MnBi_2Te_4}$ is nearly isotropic, and the magnetic anisotropy of monolayer $\mathrm{MnBi_2Te_4}$ originates from its single-ion anisotropy. We find the dominant exchange interaction is the superexchange interaction, and the direct exchange interaction is insignificant except for applying a large compressive strain (higher than 3.5%). The nearly isotropic exchange interaction is the result of the relatively weak *p*-*d* hybridization between Mn and Te atoms. We further reveal that the spin-orbit coupling effect of Te atoms can induce the changes in the local Mn-*d* states. As a result, the spin-orbit coupling effects of Mn and Te atoms jointly cause the single-ion anisotropy. Using the derived spin Hamiltonian, the Curie temperature is estimated to be about 20 K. These findings can also explain the behavior of the magnetic anisotropy in other isostructural materials, such as monolayer $\mathrm{MnSb_2Te_4}$ and $\mathrm{MnBi_2Se_4}$. In addition, the deep local Mn-*d* states imply that the magnetic state and anisotropy in monolayer $\mathrm{MnBi_2Te_4}$ are hard to manipulate. With the relatively robust magnetism, monolayer $\mathrm{MnBi_2Te_4}$ can be used as the magnetic substrate and the magnetic epitaxy of nonmagnetic materials, and to construct different magnetic heterostructures to explore quantum states such as the topological magnetoelectric effect and quantum anomalous Hall effect [57], implying a great application potential of this two-dimensional magnetic material.

ACKNOWLEDGMENTS

This work was supported by the Ministry of Science and Technology of China (Grant No. 2016YFA0301001), the National Natural Science Foundation of China (Grants No. 11674188 and No. 51788104), and the Beijing Advanced Innovation Center for Future Chip (ICFC).

[1] A. H. Castro Neto, F. Guinea, N. M. R. Peres, K. S. Novoselov, and A. K. Geim, Rev. Mod. Phys. **81**, 109 (2009).

[2] J. R. Schaibley, H. Yu, G. Clark, P. Rivera, J. S. Ross, K. L. Seyler, W. Yao, and X. Xu, Nat. Rev. Mater. **1**, 16055 (2016).

[3] M. Chhowalla, D. Jena, and H. Zhang, Nat. Rev. Mater. **1**, 16052 (2016).

[4] S. Manzeli, D. Ovchinnikov, D. Pasquier, O. V. Yazyev, and A. Kis, Nat. Rev. Mater. **2**, 17033 (2017).

[5] B. Huang, G. Clark, E. Navarro-Moratalla, D. R. Klein, R. Cheng, K. L. Seyler, D. Zhong, E. Schmidgall, M. A. McGuire, D. H. Cobden, W. Yao, D. Xiao, P. Jarillo-Herrero, and X. Xu, Nature (London) **546**, 270 (2017).

[6] C. Gong, L. Li, Z. Li, H. Ji, A. Stern, Y. Xia, T. Cao, W. Bao, C. Wang, Y. Wang, Z. Q. Qiu, R. J. Cava, S. G. Louie, J. Xia, and X. Zhang, Nature (London) **546**, 265 (2017).

[7] Z. Fei, B. Huang, P. Malinowski, W. Wang, T. Song, J. Sanchez, W. Yao, D. Xiao, X. Zhu, A. F. May, W. Wu, D. H. Cobden, J.-H. Chu, and X. Xu, Nat. Mater. **17**, 778 (2018).

[8] X. Wang, K. Du, Y. Y. F. Liu, P. Hu, J. Zhang, Q. Zhang, M. H. S. Owen, X. Lu, C. K. Gan, P. Sengupta, C. Kloc, and Q. Xiong, 2D Mater. **3**, 031009 (2016).

[9] J.-U. Lee, S. Lee, J. H. Ryoo, S. Kang, T. Y. Kim, P. Kim, C.-H. Park, J.-G. Park, and H. Cheong, Nano Lett. **16**, 7433 (2016).

[10] M. Bonilla, S. Kolekar, Y. Ma, H. C. Diaz, V. Kalappattil, R. Das, T. Eggers, H. R. Gutierrez, M.-H. Phan, and M. Batzill, Nat. Nanotechnol. **13**, 289 (2018).

[11] D. J. O'Hara, T. Zhu, A. H. Trout, A. S. Ahmed, Y. K. Luo, C. H. Lee, M. R. Brenner, S. Rajan, J. A. Gupta, D. W. McComb, and R. K. Kawakami, Nano Lett. **18**, 3125 (2018).

[12] X. Sui, T. Hu, J. Wang, B.-L. Gu, W. Duan, and M.-S. Miao, Phys. Rev. B **96**, 041410(R) (2017).

[13] B. Huang, G. Clark, D. R. Klein, D. MacNeill, E. Navarro-Moratalla, K. L. Seyler, N. Wilson, M. A. McGuire, D. H. Cobden, D. Xiao, W. Yao, P. Jarillo-Herrero, and X. Xu, Nat. Nanotechnol. **13**, 544 (2018).

[14] S. Jiang, J. Shan, and K. F. Mak, Nat. Mater. **17**, 406 (2018).

[15] Y. Deng, Y. Yu, Y. Song, J. Zhang, N. Z. Wang, Z. Sun, Y. Yi, Y. Z. Wu, S. Wu, J. Zhu, J. Wang, X. H. Chen, and Y. Zhang, Nature (London) **563**, 94 (2018).

[16] J. He, X. Li, P. Lyu, and P. Nachtigall, Nanoscale **9**, 2246 (2017).

[17] X.-L. Sheng and B. K. Nikolić, Phys. Rev. B **95**, 201402(R) (2017).

[18] Y. Li, Y. Liu, C. Wang, J. Wang, Y. Xu, and W. Duan, Phys. Rev. B **98**, 201407(R) (2018).

[19] Z. Jiang, Y. Li, W. Duan, and S. Zhang, Phys. Rev. Lett. **122**, 236402 (2019).

[20] C. Gong and X. Zhang, Science **363**, eaav4450 (2019).

[21] D. S. Lee, T.-H. Kim, C.-H. Park, C.-Y. Chung, Y. S. Lim, W.-S. Seo, and H.-H. Park, CrystEngComm **15**, 5532 (2013).

[22] M. M. Otrokov, I. I. Klimovskikh, H. Bentmann, A. Zeugner, Z. S. Aliev, S. Gass, A. U. B. Wolter, A. V. Koroleva, D. Estyunin, A. M. Shikin, M. Blanco-Rey, M. Hoffmann, A. Y. Vyazovskaya, S. V. Eremeev, Y. M. Koroteev, I. R. Amiraslanov, M. B. Babanly, N. T. Mamedov, N. A. Abdullayev, V. N. Zverev *et al.*, arXiv:1809.07389.

[23] Y. Gong, J. Guo, J. Li, K. Zhu, M. Liao, X. Liu, Q. Zhang, L. Gu, L. Tang, X. Feng, D. Zhang, W. Li, C. Song, L. Wang, P. Yu, X. Chen, Y. Wang, H. Yao, W. Duan, Y. Xu, S.-C. Zhang, X. Ma, Q.-K. Xue, and K. He, Chin. Phys. Lett. **36**, 076801 (2019).

[24] D. Zhang, M. Shi, T. Zhu, D. Xing, H. Zhang, and J. Wang, Phys. Rev. Lett. **122**, 206401 (2019).

[25] J. Li, Y. Li, S. Du, Z. Wang, B.-L. Gu, S.-C. Zhang, K. He, W. Duan, and Y. Xu, Sci. Adv. **5**, eaaw5685 (2019).

[26] M. M. Otrokov, I. P. Rusinov, M. Blanco-Rey, M. Hoffmann, A. Y. Vyazovskaya, S. V. Eremeev, A. Ernst, P. M. Echenique, A. Arnau, and E. V. Chulkov, Phys. Rev. Lett. **122**, 107202 (2019).

[27] Y. Deng, Y. Yu, M. Z. Shi, J. Wang, X. H. Chen, and Y. Zhang, arXiv:1904.11468.

[28] C. Liu, Y. Wang, H. Li, Y. Wu, Y. Li, J. Li, K. He, Y. Xu, J. Zhang, and Y. Wang, arXiv:1905.00715.

[29] J. L. Lado and J. Fernández-Rossier, 2D Mater. **4**, 035002 (2017).

[30] C. Xu, J. Feng, H. Xiang, and L. Bellaiche, npj Comput. Mater. **4**, 57 (2018).

[31] B. Shabbir, M. Nadeem, Z. Dai, M. S. Fuhrer, Q.-K. Xue, X. Wang, and Q. Bao, Appl. Phys. Rev. **5**, 041105 (2018).

[32] M. Bloch, Phys. Rev. Lett. **9**, 286 (1962).

[33] G. Kresse and J. Furthmüller, Phys. Rev. B **54**, 11169 (1996).

[34] J. P. Perdew, K. Burke, and M. Ernzerhof, Phys. Rev. Lett. **77**, 3865 (1996).

[35] P. E. Blöchl, Phys. Rev. B **50**, 17953 (1994).

[36] S. L. Dudarev, G. A. Botton, S. Y. Savrasov, C. J. Humphreys, and A. P. Sutton, Phys. Rev. B **57**, 1505 (1998).

[37] See Supplemental Material at http://link.aps.org/supplemental/10.1103/PhysRevB.100.134438 for more details about the test results of the exchange coupling matrix under more rigorous parameters, the results calculated with the U_{eff} chosen to be 4.0 and 5.0 eV, and the partial density of states of monolayer $\mathrm{CrI_3}$ and $\mathrm{CrGeTe_3}$.

[38] H. J. Xiang, E. J. Kan, S.-H. Wei, M.-H. Whangbo, and X. G. Gong, Phys. Rev. B **84**, 224429 (2011).

[39] H. Xiang, C. Lee, H.-J. Koo, X. Gong, and M.-H. Whangbo, Dalton Trans. **42**, 823 (2013).

[40] X. Ou and H. Wu, Sci. Rep. **4**, 4609 (2014).

[41] F. Zheng, J. Zhao, Z. Liu, M. Li, M. Zhou, S. Zhang, and P. Zhang, Nanoscale **10**, 14298 (2018).

[42] W.-B. Zhang, Q. Qu, P. Zhu, and C.-H. Lam, J. Mater. Chem. C **3**, 12457 (2015).

[43] J. Liu, Q. Sun, Y. Kawazoe, and P. Jena, Phys. Chem. Chem. Phys. **18**, 8777 (2016).

[44] X. Li and J. Yang, J. Mater. Chem. C **2**, 7071 (2014).

[45] N. Sivadas, M. W. Daniels, R. H. Swendsen, S. Okamoto, and D. Xiao, Phys. Rev. B **91**, 235425 (2015).

[46] I. Dzyaloshinskii, J. Phys. Chem. Solids **4**, 241 (1958).

[47] T. Moriya, Phys. Rev. **120**, 91 (1960).

[48] J. B. Goodenough, Phys. Rev. **100**, 564 (1955).

[49] J. Kanamori, J. Phys. Chem. Solids **10**, 87 (1959).

[50] K. Motida and S. Miyahara, J. Phys. Soc. Jpn **28**, 1188 (1970).

[51] N. D. Mermin and H. Wagner, Phys. Rev. Lett. **17**, 1133 (1966).

[52] T. Holstein and H. Primakoff, Phys. Rev. **58**, 1098 (1940).

[53] D. Torelli and T. Olsen, 2D Mater. **6**, 015028 (2018).

[54] B. Chen, F. Fei, D. Zhang, B. Zhang, W. Liu, S. Zhang, P. Wang, B. Wei, Y. Zhang, J. Guo, Q. Liu, Z. Wang, X. Wu, J. Zong, X. Xuedong, W. Chen, Z. Sun, D. Shen, S. Wang, Y. Zhang, M. Zhang, F. Song, H. Zhang, and B. Wang, Nat. Commun. **10**, 4469 (2019).

[55] J.-Q. Yan, S. Okamoto, M. A. McGuire, A. F. May, R. J. McQueeney, and B. C. Sales, Phys. Rev. B **100**, 104409 (2019).

[56] S. Chowdhury, K. F. Garrity, and F. Tavazza, npj Comput. Mater. **5**, 33 (2019).

[57] M. M. Otrokov, T. V. Menshchikova, M. G. Vergniory, I. P. Rusinov, A. Y. Vyazovskaya, Y. M. Koroteev, G. Bihlmayer, A. Ernst, P. M. Echenique, A. Arnau, and E. V. Chulkov, 2D Mater. **4**, 025082 (2017).